A Transient Voltage based DC Fault Line Protection Scheme for MMC based DC Grid Embedding DC Breakers

Wang Xiang, *Member, IEEE*, Junjie Zhang, Lie Xu, *Senior Member, IEEE*, Saizhao Yang, Weixing Lin, *Member, IEEE*, Jinyu Wen, *Member, IEEE*

***Abstract*—Fast and reliable DC fault detection is one of the main challenges for modular multilevel converter (MMC) based DC grid with DC circuit breakers (DCCBs). This paper extracts the high frequency components of transient voltages by wavelet transform and proposes a fault identification method based on the difference of transient voltages to identify the faulted lines for DC grids using overhead lines. Meanwhile, a faulted pole discrimination method based on the difference between the change of positive and negative pole voltages is presented. A line protection scheme including detection activation, fault identification, faulted pole discrimination and post-fault re-closing is designed. Using only the local measurements, the scheme can realize the protection of the whole line without communication and has the capability of fault resistance endurance and anti-disturbance. The proposed method is tested with a four-terminal MMC based DC grid in PSCAD/EMTDC. The selection methods of threshold values are presented and the impact of DCCB operation on the reliability of DC fault protection is analysed. Simulation results verify the fast detection and reliability of the designed DC line protection scheme.**

***Index Terms*— DC fault protection, fault identification, transient voltage, hybrid DC breaker, modular multilevel converter (MMC), post-fault re-closing.**

I. Introduction

With the increased need for renewable energy utilization and resource optimization, the modular multilevel converter (MMC) based DC grid has been a competitive candidate to integrate bulk renewable energy over long distance [1]-[3]. Different to the two-terminal HVDC systems, in a DC grid, multiple converters will feed fault currents to the faulted lines during DC faults, leading to high over-currents [4]. For the safe operation and avoiding the shutdown of the entire DC grid, it is desirable to use high-power DC circuit breakers (DCCB) to isolate the fault lines within a short period of time, e.g. a few milliseconds. As reported in [5], the four-terminal *Zhangbei* ±500kV DC grid project under construction in China requires to detect DC faults within 3ms. To facilitate fast interruption of DC faults and quick power restoration of DC grids, a reliable and selective DC fault protection scheme needs to be designed.

The traveling wave protection and boundary protection algorithms have been widely adopted in LCC-HVDC (line commutated cover based HVDC) systems [6]-[11]. However, the detection time of these DC fault protection methods does not meet the strict speed requirement of MMC-HVDC systems.

The design of protection scheme for MMC-HVDC systems includes detection activation, fault detection, fault identification and post-fault restoration [12]. Most of the existing publications focus on the design of fault detection and identification algorithms [13]-[25]. In [13] and [14], the methods using the over-current and under-voltage criteria are proposed which suffer from low selectivity. Fault detection using the derivate of DC line current is tested in [15]. However, the detection accuracy is affected by the fault resistance. As the current limiting inductor increases the electrical distance [16], reference [17] proposes the ratio of transient voltage (ROTV) detection method, in which the division of the transient voltages at converter and line side serves as the fault criterion. But a double-ended pilot method requiring the information at both ends of the DC line need to be implemented as a backup protection to guarantee selectivity, which prolongs the detection time. References [18][19] measure the rate of change of voltage (ROCOV) across the current limiting inductor to locate the faults. However, this method is sensitive to noise disturbance and fault resistance. To improve the robustness, a method based on DC reactor voltage change rate is proposed in [20] and various operating scenarios have validated its performance. However, the selection of time intervals and minimum fault detection time is difficult in a large DC grid since there are more converters feeding the fault currents. Besides, the identification of faulted pole during a pole to ground fault has not been reported. To overcome the drawbacks of time-domain protection algorithms, some signal processing methods have been proposed in [23]-[25] to extract the components in frequency domain, such as the short time Fourier transform, the lifting wavelet transform, the *S* transform and so on. The selection of the data window size, the identification of fault segments, discrimination of faulted poles and insensitivity to fault resistances and noise disturbance are presented in detail.

Regarding the post-fault restoration, an active re-closing strategy of a two-terminal HVDC system based on SB-MMC is studied in [13]. The performance of hybrid HVDC breakers

This work is sponsored by the National Key Research and Development project (2016YFB0901002) and the National Postdoctoral Program for Innovative Talents (BX201700088).

W. Xiang, J, Zhang, S. Yang, W. Lin, J. Wen are with the State Key Laboratory of Advanced Electromagnetic Engineering and Technology, Huazhong University of Science and Technology, Wuhan 430074, China. (e-mail: xiangwang1003@foxmail.com, zhangjunjie_hust@foxmail.com, weixinglin@foxmail.com, jinyu.wen@hust.edu.cn).

L. Xu is with the Department of Electronic and Electrical Engineering, University of Strathclyde, Glasgow G1 1XW, U.K. (e-mail: lie.xu@strath.ac.uk)

with the ability of three restart attempts in a two-terminal DC overhead line (OHL) transmission system is presented in [26]. However, the fault detection process is simplified and the application of the proposed methods in a DC grid needs to be further validated.

From the above literature review, it can be concluded that the overall protection procedure for MMC based DC grid has not been researched thoroughly. The theoretical basis for the algorithms was simplified and the coupled effect of the OHL has not been considered. In addition, the identification of temporary and permanent faults needs further development, and the impact of the operation of nearby DCCBs on potential false detection of the healthy lines should be analysed.

To address the above challenges, this paper proposed a DC line fault protection scheme based on high frequency components of transient voltages to identify the faulted lines and poles. The theoretical basis for fault line identification and faulted pole discrimination are presented. A re-closing strategy with two reclosing attempts is designed to quickly recover power transmission during temporary line faults.

The rest of the paper is organised as follows. Section II depicts the topology of a sample four-terminal MMC based DC grid using overhead lines. The protection principle using wavelet transform associated with phase-modal transformation method is analysed. Based on the analysis, section III proposes the protection scheme. The detection activation, DC fault identification, faulted pole discrimination and re-closing strategy are elaborated in detail. The robustness and reliability of the proposed protection scheme is verified by simulations in section IV. Finally, conclusions are drawn in section B.

II. System Layout and Fault Detection Principle

A. Topology of a Four-Terminal MMC Based DC Grid

The circuit configuration of a symmetrical monopole four-terminal MMC based DC grid is depicted in Fig. 1, where each converter employs the half bridge MMC. The DC circuit breakers CB12, CB21, CB23, CB32, CB34, CB43, CB41 and CB14 adopt the hybrid DCCB topology presented in [26]. The current limiting inductors are installed at the DC line side of DCCBs, to limit the fault current rising rate and act as the boundary of DC lines to provide high impedance paths for the high-frequency components.

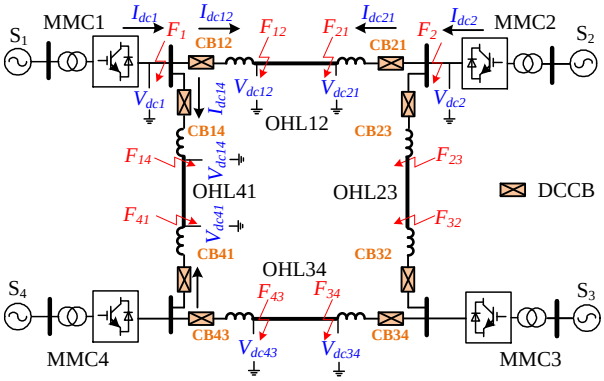

Fig. 1. The topology of a four-terminal MMC based DC grid

The pole to pole (PTP) faults and pole to ground (PTG) faults are two common faults on the DC transmission lines. The analysis and calculation of fault currents have been presented in [4] and [27] in detail. When a PTP fault occurs, the DC terminal voltage of the faulted line drops to zero quickly and the fault line current increases drastically. When a PTG fault happens, the faulted pole voltage drops to zero while the healthy pole voltage increases to two times of the rated voltage. Based on the fault characteristics, some DC fault detection criteria can be designed using time-domain methods. However, if the DC system is subject to a PTG fault with high resistance (RPTG), the change of line voltages and currents will not be significant.

B. Fault Identification Principle Based on Transient Voltages

In the event of a PTP fault at F_{12}, the frequency domain fault superposition circuit of the DC grid can be drawn as shown in Fig. 2. As shown, L_{eqi} and C_{eqi} are the equivalent inductance and capacitance of the ith MMC station. Z_{l12} is the line reactance between station 1 and 2. V_{dc1} and V_{dc12} denote the transient voltages at the DC bus side and line side, respectively. V_f represents the fault superimposed voltage source. Z_{L23}, Z_{L34}, Z_{L41} represent the equivalent reactance (including the current limiting inductance, line inductance and resistance) of the OHL 23, 34 and 41, respectively.

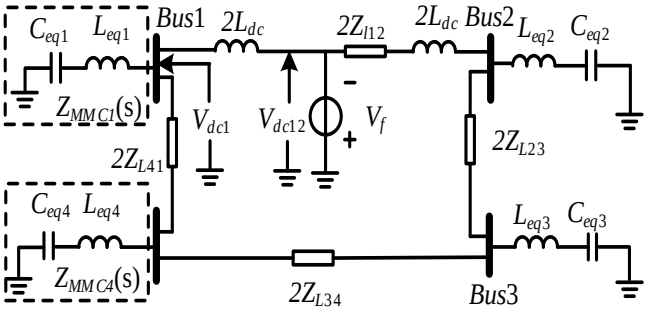

Fig. 2. The frequency domain fault superposition circuit

According to Fig. 2, since MMC 3 is far away from MMC 1, the fault current provided by MMC 3 can be neglected. Hence, the ratio of V_{dc12} and V_{dc1} can be expressed as in frequency domain.

$$\left|\frac{V_{dc12}(s)}{V_{dc1}(s)}\right| = \left|\frac{(Z_{\mathrm{MMC1}}(s)+Z_2(s))(Z_{\mathrm{MMC1}}(s)//Z_2(s)+2sL_{dc})}{Z_{\mathrm{MMC1}}(s)Z_2(s)}\right| \quad (1)$$

where $Z_2(s)=Z_{MMC4}(s)+2Z_{L41}(s)$. The equivalent reactance $Z_{MMC}(s)$ of a MMC converter can be expressed as [20]

$$Z_{\mathrm{MMC}}(s) = \frac{1}{3}(2sL_0 + \frac{N}{2sC_0}) \quad (2)$$

where L_0 and C_0 are the arm inductance and sub-module capacitance respectively. By combining (1) and (2), the magnitude frequency characteristic of the transfer function $V_{dc12}(s)/V_{dc1}(s)$ can be obtained in Fig. 3 (the parameters are listed in Table 1 and Table 2). It can be seen that the transient voltage attenuates sharply at the converter side at high frequency spectrum. Thus, the high frequency components of transient voltages between the converter side and line side can

be adopted to identify the external and internal faults (taking the protection of CB12 and CB21 as an example, the faults in OHL12 are defined as internal while in other lines are defined as external). Since the wavelet transform is widely used to extract the high frequency components, this paper uses the discrete wavelet transform to deal with the transient voltages. Denote $a_0[n]$ as the sampled signals of the transient voltage V_{dc12}(s). The approximated and detailed coefficients at j-level are as follows,

$$\begin{cases} a_j[n] = \sum_k l[k-2n]a_{j-1}[k] \\ d_j[n] = \sum_k h[k-2n]a_{j-1}[k] \end{cases} \tag{3}$$

where $l[k]$ and $h[k]$ are the low-order and high-order pass filters respectively. Actually, $d_j[n]$ represents the high frequency components of V_{dc12}(t) at j-level. Since the high-order frequency transient voltages attenuate significantly across the current limiting inductance, j can be selected as *1*. Define the integration of the square of $d_j[n]$ as the criterion to identify internal and external faults for the DCCB is described as

$$E_h = \int_0^{T_w} d_j[n]^2 \mathrm{d}t > E_{set} \tag{4}$$

where T_w is the time window and E_{set} is the setting value. Due to the requirement of fast MMC-HVDC protection, T_w is within the range of *1-3*ms. When the calculated E_{h} exceeds the setting value, it can be deemed that an internal fault occurs. Otherwise, an external fault is considered to be detected.

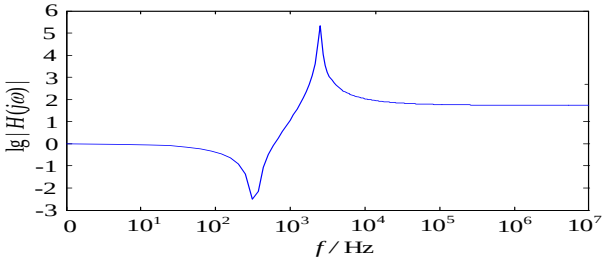

Fig. 3. Magnitude frequency characteristic curve of $|V_{dc12}(s)/V_{dc1}(s)|$.

C. Discrimination of Faulted Poles

During PTG faults, both the faulted and healthy pole voltages suffer from large fluctuation, leading to high transient energies. Thus, equation (4) cannot guarantee selectivity of faulted poles. Denote the DC line voltages at positive and negative poles as v_{1p} and v_{1n} respectively. Using the phase-modal transformation method, the pole voltages can be resolved into the line-mode component (v_{1l}) and zero-mode component (v_{10}), as shown below.

$$\begin{cases} v_{10} = \frac{1}{\sqrt{2}}(v_{1n} + v_{1p}) \\ v_{1l} = \frac{1}{\sqrt{2}}(v_{1n} - v_{1p}) \end{cases} \tag{5}$$

Denote the pre-fault values of v_{1p} and v_{1n} as $+V_{\text{dcn}}/2$ and $-V_{\text{dcn}}/2$ respectively. The pre-fault line-mode and zero-mode components can be calculated as

$$v_{10}^0 = 0, \quad v_{1l}^0 = -\frac{V_{dcn}}{\sqrt{2}} \tag{6}$$

When a PTG fault happens, according to Fig. 4(a), the instantaneous boundary conditions are as follows.

$$v_{1p} = R_g i_{1p}, \quad i_{1n} = 0 \tag{7}$$

where R_g is the fault resistance. Transforming the current into line and zero modes yields,

$$\begin{cases} i_{10} = \frac{1}{\sqrt{2}}(i_{1n} + i_{1p}) \\ i_{1l} = \frac{1}{\sqrt{2}}(i_{1n} - i_{1p}) \end{cases} \tag{8}$$

Based on (5)-(8), the instantaneous boundary can be re-written as,

$$\begin{cases} v_{1l} - v_{10} = R_g(i_{1l} - i_{10}) \\ i_{10} + i_{1l} = 0 \end{cases} \tag{9}$$

Thus, the modal circuit can be obtained as depicted in Fig. 4 (b), where Z_1 and Z_0 are the positive and zero sequence impedances of the HVDC lines (Z_0>Z_1[28]).

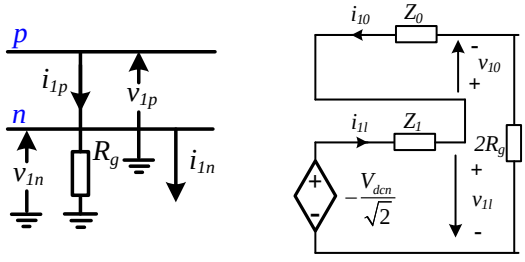

(a) A positive PTG fault (b) Modal circuit

Fig. 4. Modal circuit during positive PTG fault.

From Fig. 4 (b), the line-mode and zero-mode components can be solved as follows.

$$\begin{cases} v_{10} = -\frac{V_{dcn}}{\sqrt{2}} \frac{Z_0}{(Z_0 + Z_1 + 2R_g)} \\ v_{1l} = -\frac{V_{dcn}}{\sqrt{2}} \frac{Z_0 + 2R_g}{(Z_0 + Z_1 + 2R_g)} \end{cases} \tag{10}$$

Then, the change of v_{10} and v_{1l} are expressed as,

$$\begin{cases} \Delta v_{10} = v_{10}^0 - 0 = -\frac{V_{dcn}}{\sqrt{2}} \frac{Z_0}{(Z_0 + Z_1 + 2R_g)} \\ \Delta v_{1l} = v_{1l}^0 - (-\frac{V_{dcn}}{\sqrt{2}}) = \frac{V_{dcn}}{\sqrt{2}} \frac{Z_1}{(Z_0 + Z_1 + 2R_g)} \end{cases} \tag{11}$$

Considering (5) and (11), the change of v_{1p} and v_{1n} are

$$\begin{cases} \Delta v_{1p} = \frac{\Delta v_{10} - \Delta v_{1l}}{\sqrt{2}} = -\frac{V_{dcn}(Z_0 + Z_1)}{2(Z_0 + Z_1 + 2R_g)} \\ \Delta v_{1n} = \frac{\Delta v_{10} + \Delta v_{1l}}{\sqrt{2}} = -\frac{V_{dcn}(Z_0 - Z_1)}{2(Z_0 + Z_1 + 2R_g)} \end{cases} \tag{12}$$

It can be concluded from (12) that, the change of v_{1p} is larger than the change of v_{1n}. Therefore, within a certain time window, the integration of the voltage change of the faulted pole is always larger than that of the healthy pole. Hence, the discrimination criterion for the faulted pole can be designed as follows,

$$\left| \int_0^{T_w} \Delta v_{1p} dt \right| - \left| \int_0^{T_w} \Delta v_{1n} dt \right| = \Delta s, \begin{cases} \Delta s > \Delta set, \textit{positive pole} \\ \Delta s < -\Delta set, \textit{negative pole} \end{cases} \tag{13}$$

where Δs is the subtraction of the integration of the change of

positive and negative pole voltages. *Δset is* the setting threshold. On detecting *Δs* exceeds *Δset*, a positive PTG fault is detected. On detecting *Δs* is less than *-Δset*, a negative PTG fault is detected. Otherwise, a PTP fault is recognized.

III. Design of DC Fault Protection Scheme

A. Start-up Element and Re-closing Sequence

To avoid frequent activation during normal operating conditions, a start-up element is designed to trigger the protection scheme. Since the DC line voltage decreases significantly during DC faults, a voltage derivative criterion can be employed.

$$dV_1 / dt < DV_{dc} \tag{14}$$

where DV_{dc} is the threshold, which should be set to be able to discriminate the normal operating conditions and DC faults.

When the fault identification and faulted pole discrimination have been accomplished, the tripping orders will be sent to the DCCBs to isolate the fault lines. After the isolation of the fault lines, the DCCBs need to be re-closed to restore the power transmission. Therefore, a post-fault recovery strategy is designed in Fig. 5.

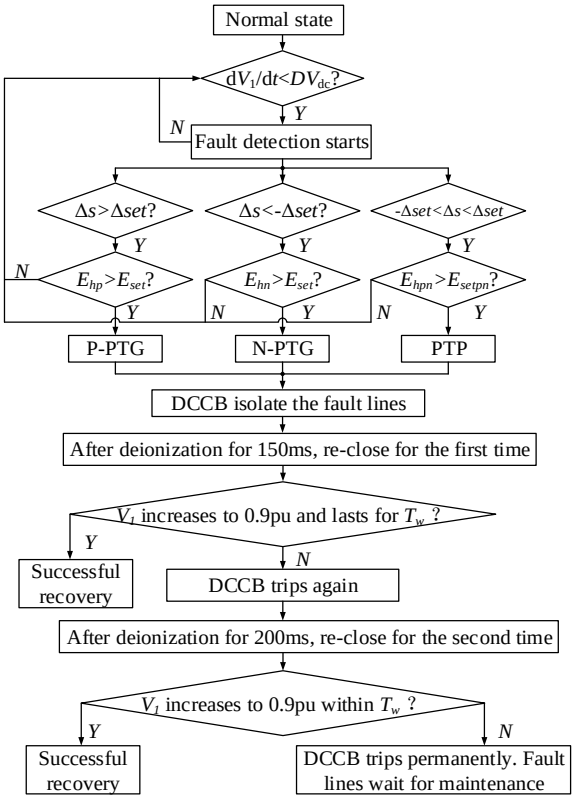

Fig. 5. Flow-chart of overall protection scheme.

As can be seen, when the DC fault is cleared, the DCCBs are re-closed for the first time after deionization for 150ms. If the DC line voltage V_1 increases to 0.9p.u. and lasts for T_w, it is deemed that the fault has been cleared and the power transmission can be restored. Otherwise, the DCCBs will be tripped again. Subsequently, DCCBs will re-close for the second time. If the line voltage is still below 0.9p.u., the fault is considered to be permanent. Thus, DCCBs trip permanently and the faulty segments wait for manual maintenance.

B. Overall Protection Scheme

Based on the aforementioned analysis, the overall protection scheme is depicted in Fig. 5. Once the detected derivative of DC line voltage is less than the threshold (DV_{dc}), the protection scheme activates. Since the setting thresholds of E_h for PTG and PTP faults are different, it is necessary to identify which fault occurs. As a result, the pole discrimination algorithm is activated first. In Fig. 5, E_{hp}, E_{hn} and E_{hpn} represent the transient energies of the positive pole voltage, negative pole voltage and PTP DC line voltage, respectively. Denote E_{set} and E_{setpn} as the setting thresholds of transient energies of the pole voltage and pole to pole voltage respectively. On detecting *Δs>Δset* and $E_{hp}>E_{set}$, a positive PTG fault is identified. On detecting *Δs<-Δset* and $E_{hn}>E_{set}$, a negative PTG fault is identified. On detecting *-Δset< Δs<Δset* and $E_{hpn}>E_{setpn}$, a PTP fault is identified. When the fault type is distinguished, the corresponding DCCBs are tripped and after DC line deionization, the re-closing sequence starts.

IV. Simulation Validations

In order to verify the feasibility of the proposed protection scheme, the four-terminal MMC based DC grid shown in Fig. 1 is simulated in PSCAD/EMTDC. MMC1 controls the DC voltage and reactive power while MMC2-4 control the active and reactive power. The power flow and current direction from AC system injected into DC system is defined as positive, and the rated power of the converters are as follows. MMC1 transmits 0.1p.u. reactive power. MMC2 transmits 0.9p.u. active and 0.15p.u. reactive power. MMC3 transmits 0.9p.u. active and 0.1p.u. reactive power. MMC4 transmits -0.9p.u. active and 0.1p.u. reactive power.

The main parameters of the converters and AC systems are listed in Table 1and Table 2 respectively. The lengths of the overhead line are also shown in Table 2.

Table 1 Parameters of MMCs

Station	Capacity /MW	Rated DC voltage/kV	Arm inductance /mH	SM capacitance /mF	Number of SMs per arm
MMC1	3000	±500	96	15	200
MMC2	2000	±500	144	10	200
MMC3	2500	±500	115	12.5	200
MMC4	1500	±500	192	8	200

Table 2 Parameters of AC system and DC systeM

AC system	Rated AC voltage/kV	Short circuit capacity/MVA
S1	500	31500
S2	500	15000
S3	500	15000
S4	500	15000
DC system	**Length of OHL**	**Limiting inductance/mH**
OHL12	240km	150
OHL12	100km	150
OHL23	200km	150
OHL34	120km	150

To avoid false activation of the protection, DV_{dc} is set as -1000kV/ms. The sampling frequency is chosen as 20kHz. To make a trade-off between detection speed and reliability, the time window T_w is selected as 1.5ms. The wavelet transform is set as *1*-level and the corresponding frequency is 5kHz-10kHz. The mother wavelet is selected as *sym8* [29].

A. Determination of Setting Values

For DCCBs 12 and 21, the internal DC faults in OHL12 should be correctly identified while no protection should be activated during external faults. The most severe external faults for them are the DC bus faults at the DC terminals of MMC1 and MMC2 respectively, which are labelled as F_1 and F_2 in Fig. 1. Scanning the DC bus faults and line faults (PTP) along OHL12, the measured transient voltages and energies $\Delta s12$, $\Delta s21$, E_{hpn12} and E_{hpn21} are listed in Table 3.

Table 3 Measured values under different fault location (PTP fault)

Location	Δs12	Δs21	E_{hpn12}	E_{hpn21}
MMC1 DC bus	-0.6	0.1	41	**48**
F_{12}	-0.04	-0.03	2170	6780
1/8 of OHL12	0.1	0.002	15165	6907
1/4 of OHL12	0.05	-0.1	7540	7193
1/2 of OHL12	0.001	-0.001	7679	7679
3/4 of OHL12	0.05	-0.05	7238	7584
7/8 of OHL12	0.1	0.1	6972	13575
F_{21}	0.2	-0.15	6867	2206
MMC2 DC bus	0.05	-2.5	**48**	41

Due to the PTP fault, the difference between the integration of the change of positive and negative pole voltages is small, leading to small values of $\Delta s12$ and $\Delta s12$, as shown in Table 3. With the increase of the distance between the CB12 and the fault location along OHL12, E_{hpn12} increases first but then decreases. Similar results can be observed for E_{hpn21}. It should also be noted that the E_h during the internal faults is much larger than that during the external faults. As a result, the method of using E_h can successfully identify the external and internal faults.

Scanning the metallic PTG faults at the same locations, $\Delta s12$, $\Delta s21$, E_{hp12} and E_{hp21} are obtained as shown in Table 4. Since the change of the positive pole voltage is larger than that of the negative pole voltage, $\Delta s12$ and $\Delta s21$ are much larger than those in Table 3, which verifies that equation (13) is able to identify PTP and PTG faults. The same as the results in Table 3, the values of E_{hp12} and E_{hp21} during internal faults are much larger compared with external faults.

Table 4 Measured values under different fault location (PTG fault)

Location	Δs12	Δs21	E_{hp12}	E_{hp21}
MMC1 DC bus	100	70	**9**	0.005
F_{12}	380	**300**	544	386
1/8 of OHL12	380	335	3054	505
1/4 of OHL12	390	325	1240	450
1/2 of OHL12	320	320	460	460
3/4 of OHL12	330	400	480	1260
7/8 of OHL12	330	380	480	3050
F_{21}	**310**	385	390	540
MMC2 DC bus	80	115	0.007	**8**

The thresholds of $\Delta s12$ *and* $\Delta s21$ can be set as $k_f * \Delta s_{min}$ where Δs_{min} is the minimum value of $\Delta s12$ and $\Delta s21$ under internal PTG faults. The coefficient k_f is used to improve the reliability enduring different fault resistances, which is selected as 0.5 in this paper. According to the simulation results, the thresholds of $\Delta s12$ and $\Delta s21$ are 155 and 150 respectively.

The thresholds of E_{hp12} *and* E_{hp21} can be set as $k_r * E_{hpmax}$, where E_{hpmax} is the maximum value of E_{hp12} and E_{hp21} under external PTG faults. k_r is also used to improve the reliability, which is selected as 10 in this paper to leave some margin. According to the simulation results, the thresholds of E_{hp12}, E_{hp21}, E_{hpn12} and E_{hpn21} are 90, 80, 480 and 480, respectively.

Using the setting methods, all the thresholds can be obtained as depicted in Table 5.

Table 5 Setting thresholds of DC line protections

Protection	Δ_{set} ($-\Delta_{set}$)	E_{set}	E_{setpn}
*DCCB*12	155	90	480
*DCCB*21	150	80	480
*DCCB*23	110	80	650
*DCCB*32	110	80	650
*DCCB*34	145	80	600
*DCCB*43	145	80	600
*DCCB*41	160	80	670
*DCCB*14	160	80	670

B. Response to Temporary PTP Fault

To validate the protection scheme and analyse the impact of DCCB operation on healthy lines during fault tripping and post-fault re-closure, a temporary metallic PTP fault is applied at F_{34} at 2s. The simulation results are shown in Fig. 6 (a)-(l).

Fig. 6(a) shows that dV_{dc34}/dt and dV_{dc43}/dt drop drastically and exceed the threshold (-1000kV/ms). Thus, the protection sequence of DCCBs 34 and 43 activates. As can be seen in Fig. 6(b) and (c), Δs is within the range of (*-80*, *80*) and E_{hpn34}, E_{hpn43} exceed the threshold (*600*). Thus, a PTP fault is detected, and the tripping orders are sent to DCCBs 34 and 43 at 2.0015s and 2.002s respectively, as shown in Fig. 6(d) and (e) (*1* stands for closing while *0* stands for tripping). After 150ms deionization, DCCBs 34 and 43 re-close. The line voltages V_{dc34} and V_{dc43} exceed 0.9p.u. within 1.5ms, which are shown in Fig. 6(f). Thus, the PTP fault is considered as temporary. Since the stray capacitors in OHL34 discharge fully during the fault, the reclose of DCCBs will cause oscillation in DC terminal voltages and currents, as shown in Fig. 6(g) and (h). For DCCBs 23, 32, 41 and 14, although DCCBs 34 and 43 have been tripped, the DC voltage derivatives still exceed -1000kV/ms. Thus, the protection scheme activates. However, the transient energies (E_{hpn23}, E_{hpn32}, E_{hpn41}, E_{hpn14}) are within the safety range and thus, the protection is executed and DCCBs 23, 32, 41 and 14 are not tripped, as can be seen in Fig. 6(i)-(l).

From Fig. 6, it can be seen that the protection scheme of the healthy lines might be activated due to the tripping of nearby DCCBs. To further investigate the impact of DCCB operation on the reliability of protection scheme, F_{12}, F_{21}, F_{23}, F_{32}, F_{43}, F_{41}, F_{14} faults are applied. The maximum transient energies E_{hpn} during the entire process are listed in Table 6.

As can be seen, the internal PTP faults result in large value of E_h. While during external faults, E_{hpn} is rather small. Compared with the thresholds shown in Table 5, the internal faults will successfully activate the protection algorithm, while the external faults will not lead to false detection.

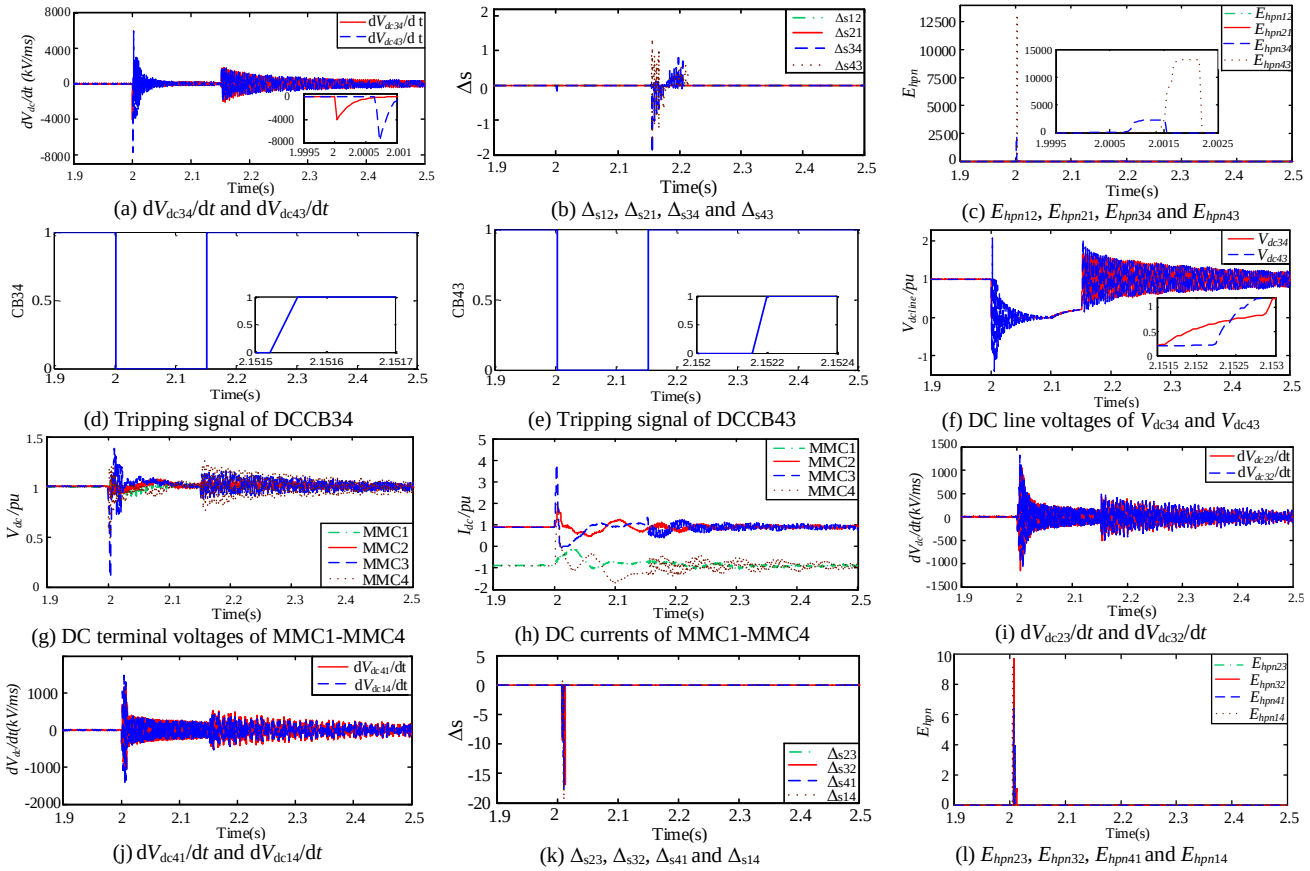

(a) dV_{dc34}/dt and dV_{dc43}/dt (b) Δ_{s12}, Δ_{s21}, Δ_{s34} and Δ_{s43} (c) E_{hpn12}, E_{hpn21}, E_{hpn34} and E_{hpn43}

(d) Tripping signal of DCCB34 (e) Tripping signal of DCCB43 (f) DC line voltages of V_{dc34} and V_{dc43}

(g) DC terminal voltages of MMC1-MMC4 (h) DC currents of MMC1-MMC4 (i) dV_{dc23}/dt and dV_{dc32}/dt

(j) dV_{dc41}/dt and dV_{dc14}/dt (k) Δ_{s23}, Δ_{s32}, Δ_{s41} and Δ_{s14} (l) E_{hpn23}, E_{hpn32}, E_{hpn41} and E_{hpn14}

Fig. 6. Simulation waveforms of temporary PTP fault (fault resistance is 0Ω).

Table 6 Maximum transient energies during PTP faults

Fault location	E_{hpn12}	E_{hpn21}	E_{hpn23}	E_{hpn32}	E_{hpn34}	E_{hpn43}	E_{hpn41}	E_{hpn14}
F_{12}	**2170**	**6780**	4	4	0	0	0	0
F_{21}	**6867**	**2206**	4	23	0	0	4	4
F_{23}	15	13	**2251**	**14360**	6	6	0	0
F_{32}	27	11	**14420**	**2255**	4	9	0	0
F_{34}	0	0	4	9	**2252**	**13143**	6	9
F_{43}	0	0	1	2	**13036**	**2227**	0	0
F_{41}	75	72	0	0	0	0	**2228**	**8218**
F_{14}	0	0	0	0	0	0	**8204**	**2221**

To further validate the robustness of the proposed protection scheme during RPTP faults, a temporary PTP fault with 100Ω resistance is applied at 2s. The simulation results are shown in Fig. 7 (a)-(f).

Due to the fault resistance, the drop of the DC line voltage is not as severe as that with the metallic fault. Thus, only dV_{dc34}/dt and dV_{dc43}/dt exceed the threshold and the start-up element activates, as shown in Fig. 7(a). Fig. 7(b)-(c) show that Δs is within the range of (*-80*, *80*) and only E_{hpn34}, E_{hpn43} exceed the threshold (E_{hpn34}=1535, E_{hpn43}=8960). Thus, a PTP fault in OHL34 is detected. After 150ms deionization, DCCBs 34 and 43 re-close and the line voltages V_{dc34} and V_{dc43} shown in Fig. 7(d) exceed 0.9p.u. after 1.5ms. The power transmission restores, as shown in Fig. 8(e)-(f).

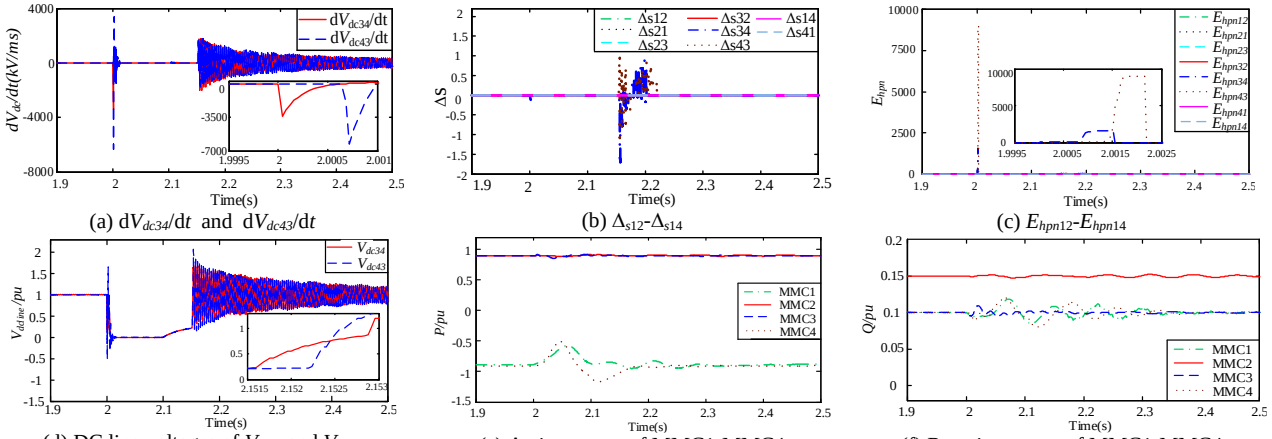

(a) dV_{dc34}/dt and dV_{dc43}/dt (b) Δ_{s12}-Δ_{s14} (c) E_{hpn12}-E_{hpn14}

(d) DC line voltages of V_{dc34} and V_{dc43} (e) Active power of MMC1-MMC4 (f) Reactive power of MMC1-MMC4

Fig. 7. Simulation waveforms of temporary PTP fault (fault resistance is 100Ω).

C. Response to Temporary PTG Fault

To test the faulted pole discrimination algorithm, a temporary PTG fault with 200Ω resistance is applied at the middle of OHL12 of the positive pole at 2s. The simulation results are shown in Fig. 8.

Fig. 8(a) show that both dV_{dc12}/dt and dV_{dc21}/dt exceed the threshold (-1000kV/ms), and thus the protection scheme of DCCBs 34 and 43 activates. As can be seen in Fig. 8(b)-(c), $\Delta s12=\Delta s12>155$ and $E_{hp12}=E_{hp21}>90$. Thus, a positive PTG fault is detected. Fig. 8(d)-(f) show the DC voltage, active power and reactive power during re-closing. The system restores power transmission quickly. It can be seen that the proposed pole discrimination is able to endure high fault resistance.

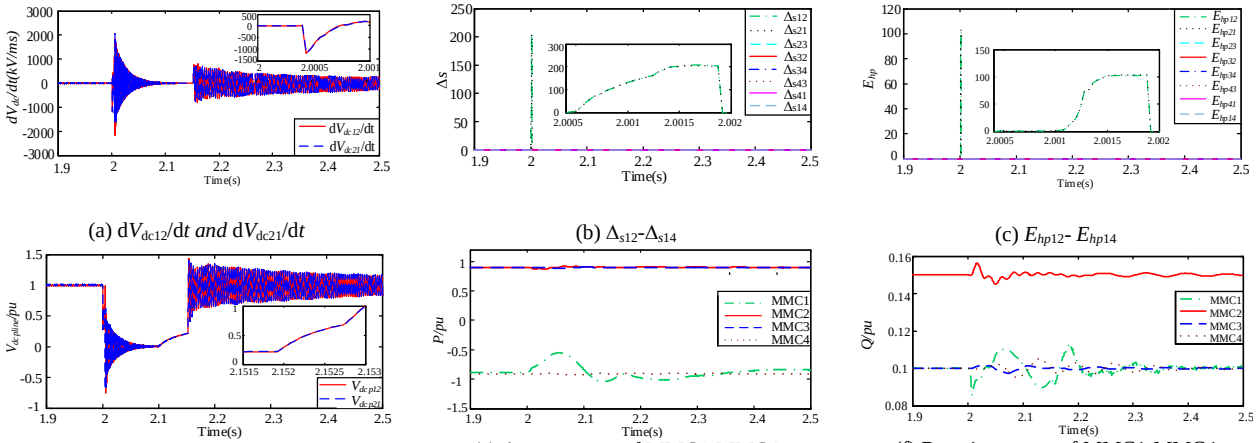

(a) dV_{dc12}/dt *and* dV_{dc21}/dt (b) Δ_{s12}-Δ_{s14} (c) E_{hp12}- E_{hp14}

(d) DC line voltages of V_{dcp12} and V_{dcp21} (e) Active power of MMC1-MMC4 (f) Reactive power of MMC1-MMC4

Fig. 8. Simulation waveforms of temporary PTG fault (fault resistance is 200Ω).

D. Response to Permanent PTP Fault and Impact of Re-closing

Simulations are carried out to test the re-closing strategy during a permanent metallic PTP fault at the middle point of OHL41 at 2s, and the results are shown in Fig. 9(a)-(i).

Fig. 9(a) shows that dV_{dc41}/dt and dV_{dc14}/dt exceed the threshold and the protection scheme of DCCBs 14 and 41 activates. Fig. 9(b)-(c) show that $\Delta s41=\Delta s14=0.12$ and $E_{hpn41}=E_{hpn41}=15000$. Thus, a PTP fault is detected. DCCBs 14 and 41 are tripped to isolate the fault line. After 150ms deionization, DCCBs 14 and 41 attempt to re-close. Since the fault still exists, the DC line voltage is below 0.9p.u. and the fault current increases again. Then, DCCBs 14 and 41 trip again. After 200ms deionization, DCCBs 14 and 41 attempt to re-close for the second time. On detecting V_{dc41} and V_{dc14} is still below 0.9p.u., the fault is considered as permanent. DCCBs 14 and 41 trip permanently. After the isolation of OHL41, the remaining parts restore rated power transmission, as shown in Fig. 9(f)-(i).

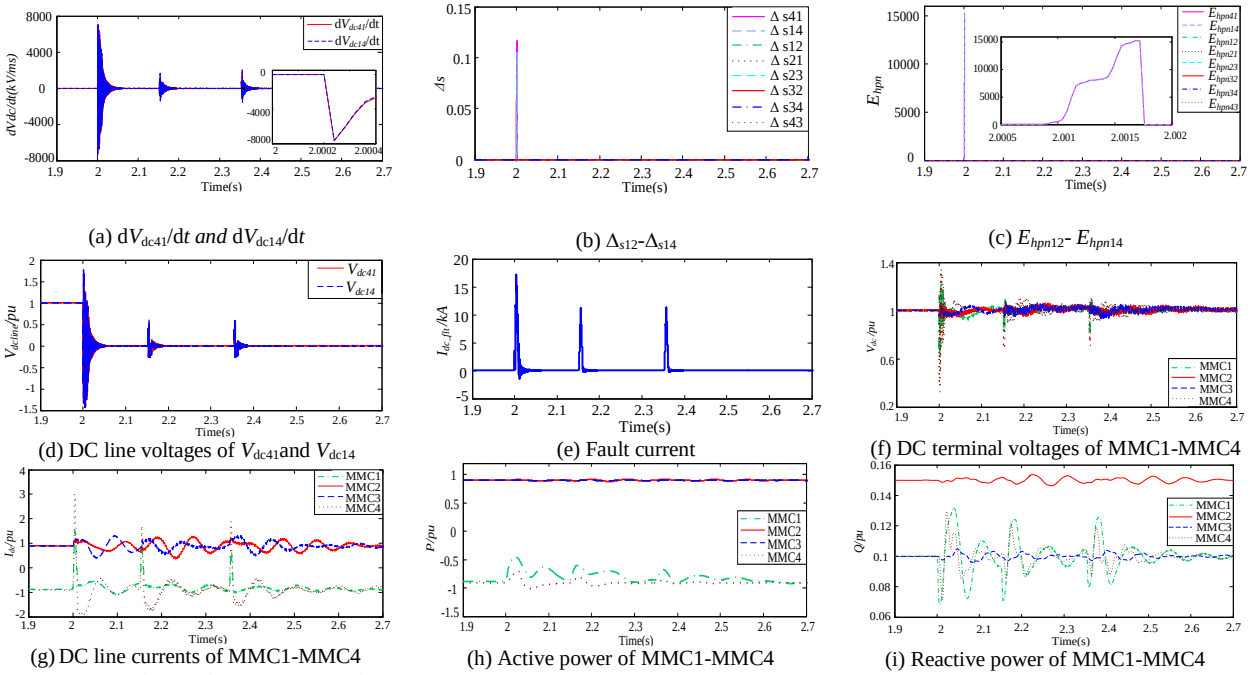

(a) dV_{dc41}/dt *and* dV_{dc14}/dt (b) Δ_{s12}-Δ_{s14} (c) E_{hpn12}- E_{hpn14}

(d) DC line voltages of $V_{dc41}$and V_{dc14} (e) Fault current (f) DC terminal voltages of MMC1-MMC4

(g) DC line currents of MMC1-MMC4 (h) Active power of MMC1-MMC4 (i) Reactive power of MMC1-MMC4

Fig. 9. Simulation waveforms of permanent PTP fault.

V. Robustness Evaluation

A. Influence of Change of Operating Conditions and blocking of Converter

Further studies are carried out to test the impact of fast change of operating conditions, e.g. active and reactive power change, on the proposed protection strategy. At 2s, the respective active and reactive power orders of MMC2 step from 0.9p.u. and 0.15p.u. to 0. The active power order of MMC4 steps from -0.9p.u. to -0.7p.u. at 2.2s. The active power order of MMC3 steps from 0.9p.u. to 0.7p.u. at 2.4s. At 2.5s, MMC2 is blocked. At 3.5s, a temporary PTP fault is applied at F_{23}. The simulation results are shown in Fig. 10.

Fig. 10(a)-(b) show the active power and reactive power. They match the power orders well. Fig. 10(c)-(d) show the DC terminal voltages and line currents. As can be seen, there are some transients during the change of operating conditions. However, from Fig. 10(e)-(g), it can be seen that the transients will not cause the false activation of the protection scheme. At 3.5s, since a PTP fault happens, it triggers the protection scheme. Thus, DCCBs 23 and 32 are tripped to isolate the fault line. The waveforms of the fault current and V_{dc23}, V_{dc32} are shown in Fig. 10 (h)-(i).

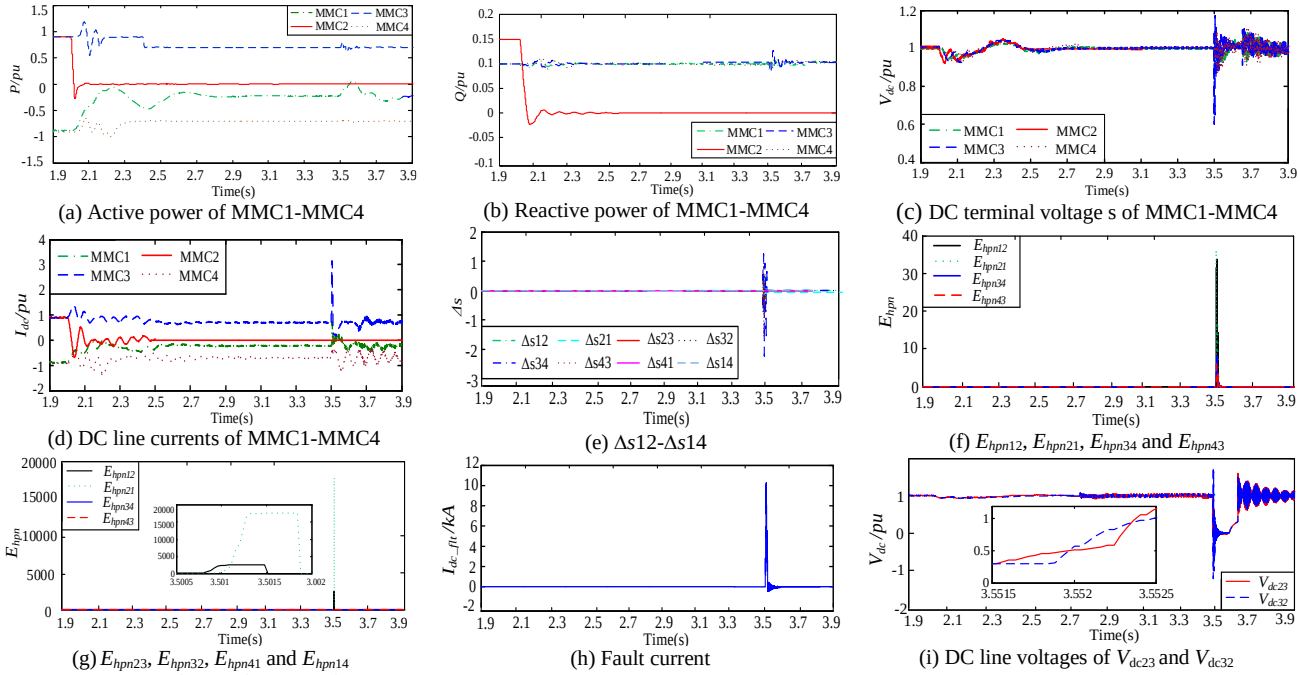

(a) Active power of MMC1-MMC4 (b) Reactive power of MMC1-MMC4 (c) DC terminal voltage s of MMC1-MMC4

(d) DC line currents of MMC1-MMC4 (e) Δs12-Δs14 (f) E_{hpn12}, E_{hpn21}, E_{hpn34} and E_{hpn43}

(g) E_{hpn23}, E_{hpn32}, E_{hpn41} and E_{hpn14} (h) Fault current (i) DC line voltages of V_{dc23} and V_{dc32}

Fig. 10. Simulation waveforms of change of operating conditions.

B. Response to AC faults

To verify the impact of AC faults on the reliability of the algorithm, a solid phase A-to-ground fault is applied at 2s. Fig. 11 (a) and (b) show the response to AC fault at the primary and secondary side of the MMC 4 interface transformer. As can be seen, the voltage derivatives are around zero and thus, the AC faults will not cause false activation of the protection scheme.

C. Influence of Noise

At 2s, a positive pole–to-ground fault is applied at F_{32}. To test the robustness under noisy environment, a 35db noise was added in the measured signals and the simulation results are shown in Fig. 12.

As can be seen in Fig. 12(a)-(b), the dV_{dc32}/dt and dV_{dc23}/dt exceed the threshold and the protection schemes of DCCBs 32 and 23 activate, whereas the nearby DCCBs will not activated. Fig. 12 (c)-(d) show that $\Delta s23=300$, $\Delta s32=350$ and E_{hpn23}= 400, E_{hpn32}=800. Thus, a positive PTG fault is detected, and DCCBs 23 and 32 are tripped to isolate the fault line.

To further test the influence of different levels of noise, a 25db noise is applied at the same place. The simulation results are shown in Fig. 13.

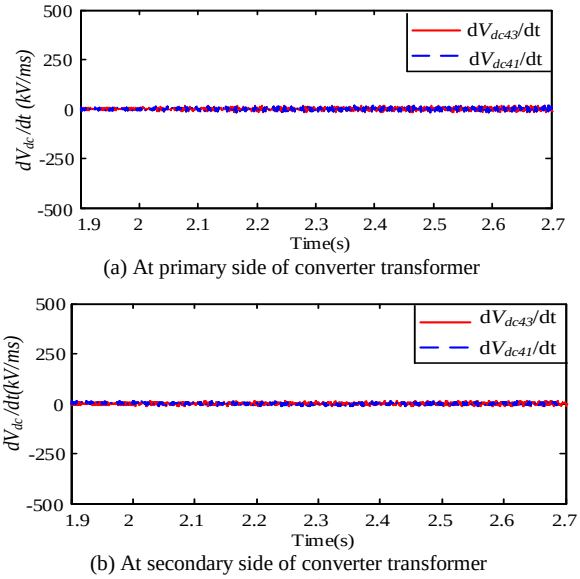

(a) At primary side of converter transformer

(b) At secondary side of converter transformer

Fig. 11. Voltage derivative during an AC fault

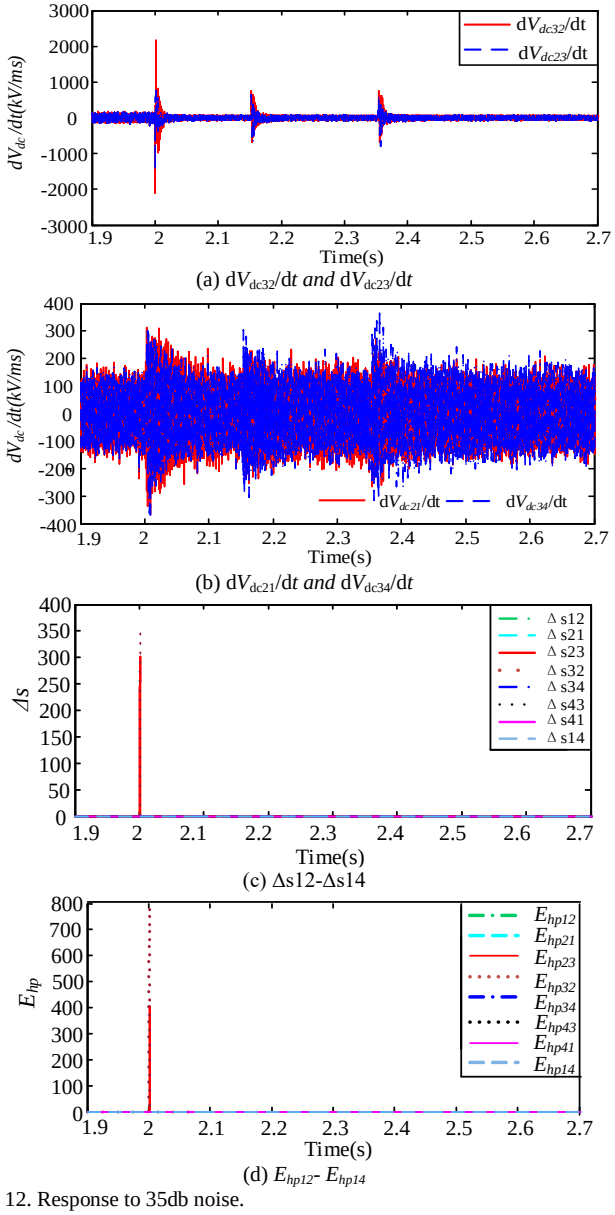

Fig. 12. Response to 35db noise.

As can be seen in Figs. 13 (a)-(b), the fluctuation is much larger compared with Fig. 12. However, only dV_{dc32}/dt and dV_{dc23}/dt exceed the threshold leading to the activation of the protection schemes of DCCBs 32 and 23. Figs. 13 (c)-(d) show that a positive PTG fault is detected.

D.Time Delay Evaluation

Detection time delay is vital for the protection scheme, and varies with the change of fault scenarios, such as fault types, fault resistances, fault distances and so on. In this paper, extensive faults have been scanned along the overhead lines and the longest time observed is 2.2ms which happens at DCCB 43 when a PTP fault is applied at F_{34}.

VI. Conclusion

A DC fault protection scheme for MMC based DC grids using OHL is proposed in this paper. The derivative of DC line voltage is adopted as the start-up element. The difference between the integration of positive and negative pole voltage variations combined with the integration of the square of transient voltages are used to discriminate the faulty lines and poles. A post-fault re-closing strategy is proposed to deal with temporary and permanent faults. The proposed method only requires local measurements with no need for fast telecommunication. The simulations have demonstrated that the protection scheme is able to identify PTP, PTG faults with high selectivity and strong robustness against fault resistance within 2-3ms. The protection scheme is independent of the power flow direction, and the operation of DCCBs during DC fault tripping and post-fault re-closing will not cause false detection on healthy lines. The proposed protection scheme provides an attractive approach for application in future DC grids.

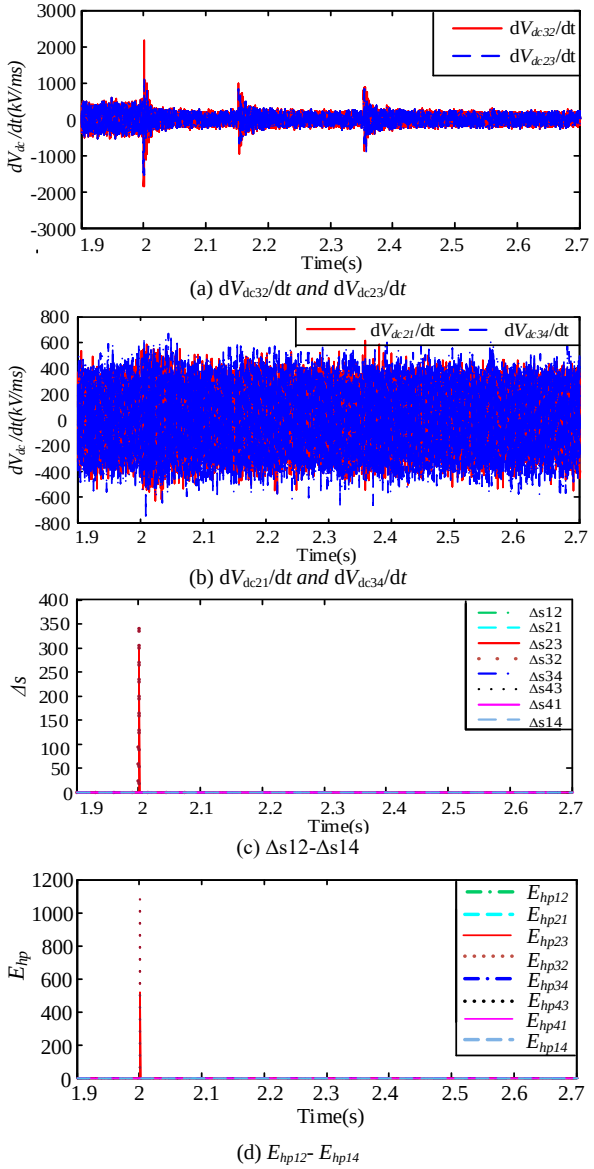

Fig. 13. Response to 25db noise.

Appendix

The overhead DC transmission lines are modelled based on the frequency dependent (phase) model using in the PSCAD software and Fig. 14 illustrates the configuration.

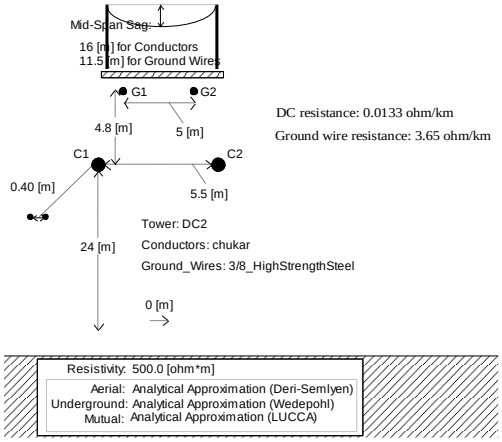

Fig. 14. Configuration of the overhead lines.

REFERENCES

[1] O. D. Adeuyi, M. Cheah-Mane, J. Liang, N. Jenkins, "Fast Frequency Response from Offshore Multi-terminal VSC-HVDC Schemes," *IEEE Trans. Power Del.*, vol. 32, no. 6, pp. 2442-2452, Dec. 2017.

[2] W. Xiang, W. Lin, L. Xu, J. Wen, "Enhanced Independent Pole Control of Hybrid MMC-HVDC System," *IEEE Trans. Power Del.*, early access, DOI: 10.1109/TPWRD.2017.2715040.

[3] Y. Li, G. Tang, J. Ge, Z. He, "Modeling and Damping Control of Modular Multilevel Converter Based DC Grid," *IEEE Trans. on Power Syst.*, vol. 33, no. 1, pp. 723-735, Jan. 2018.

[4] C. Li, C. Zhao, J. Xu, et al, "A Pole-to-Pole Short-Circuit Fault Current Calculation Method for DC Grids," *IEEE Trans. on Power Syst.*, vol. 32, no. 6, pp. 4943-4953, Nov. 2017.

[5] X. Dong, L. Tang, S. Shi, Y. Qiu, M. Kong, H. Pang, "Configuration Scheme of Transmission Line Protection for Flexible HVDC Grid," *Power System Technology*, vol. 42, no.6, pp. 1752-1759, 2018.

[6] X. Liu, A. H. Osman, O. P. Malik, "Hybrid traveling wave/boundary protection for monopolar HVDC line," *IEEE Trans. Power Del.*, vol. 24, no. 2, pp. 569–578, Apr. 2009.

[7] X. Liu, A. H. Osman, O. P. Malik, "Real-Time implementation scheme for bipolar HVDC line using FPGA," *IEEE Trans. Power Del.*, vol. 26, no. 1, pp. 101–108, Jan. 2011.

[8] S. Gao, X. Chu, Q. Shen, et al, "A novel whole-line quick-action protection principle for HVDC transmission lines using one-end voltage," *Int. Journal of Electr. Power & Energ. Syst.*, vol. 65, pp. 262-270, 2015.

[9] G. Song, X. Chu, S. Gao, et al, "A new whole-line quick-action protection principle for HVDC transmission lines using one-end current," *IEEE Trans. Power Del.*, vol.30, no.2, pp. 599–607, Apr. 2015.

[10] M. Xu, Z. Cai, K. Han, et al, "A sensitive and high-speed traveling wave protection scheme for HVDC transmission line," *Int. Trans. Electr. Energ. Syst.*, vol.25, pp. 393–404, 2015.

[11] F. Kong, Z. Hao, S. Zhang, B. Zhang, "Development of A Novel Protection Device for Bipolar HVDC Transmission Lines," *IEEE Trans. Power Del.*, vol.29, no.5, pp. 2270-2278, Oct. 2014.

[12] D. S. Loume, A. Bertinato, B. Raison, et al, "A multi-vendor protection strategy for HVDC grids based on low-speed DC circuit breakers," *presented in 13th IET International Conf. on AC and DC Power Transm.*, Manchester, UK, 2017, pp. 1-6.

[13] W. Xiang, W. Lin, T. An, J. Wen, Y. Wu, "Equivalent electromagnetic transient simulation model and fast recovery control of overhead VSC-HVDC based on SB-MMC," *IEEE Trans. Power Del.*, vol.32, no.2, pp. 778-788, Apr. 2017.

[14] E. Kontos, T. Schultz, L. Mackay, L. Ramirez-Elizondo, C. M. Franck, P. Bauer, "Multi-Line Breaker for HVDC Applications," *IEEE Trans. Power Del.*, early access, DOI: 10.1109/TPWRD.2017.2754649.

[15] N. Geddada, Y. M. Yeap, A. Ukil, "Experimental Validation of Fault Identification in VSC Based DC Grid System," *IEEE Trans. Ind. Electron.*, early access, DOI: 10.1109/TIE.2017.2767560.

[16] I. Jahn; N. Johannesson; S. Norrga, "Survey of methods for selective DC fault detection in MTDC grids," *presented in 13th IET International Conf. on AC and DC Power Transm.*, Manchester, UK, 2017, pp. 1-7.

[17] J. Liu, N. Tai, C. Fan, "Transient-Voltage Based Protection Scheme for DC Line Faults in Multi-terminal VSC-HVDC System," *IEEE Trans. Power Del.*, vol.32, no.3, pp. 1483-1494, Jun. 2017.

[18] J. Sneath, A. Rajapakse, "Fault detection and Interruption in an earthed HVDC grid using ROCOV and hybrid DC breakers," *IEEE Trans. Power Del.*, vol.31, no.3, pp. 973-981, Jun. 2016.

[19] W. Lin, D. Jovcic, S. Nguefeu, et al, "Coordination of MMC converter protection and DC line protection in DC grids," *presented in IEEE Power and Energy Society General Meeting*, 2016, pp. 1-5.

[20] R. Li, L. Xu, L. Yao, "DC fault detection and location in meshed multi-terminal HVDC systems based on DC reactor voltage change rate," *IEEE Trans. Power Del.*, vol.32, no.3, pp. 1516-1626, Jun. 2017.

[21] X. Zheng, N. Tai, S. J. James, G. Yang, "A Transient Protection Scheme for HVDC Transmission Line," *IEEE Trans. Power Del.*, vol.27, no.4, pp. 2278-2285, Oct. 2012.

[22] X. Dong, S. Luo, S. Shi, et al, "Implementation and application of practical traveling-wave-based directional protection in UHV transmission lines," *IEEE Trans. Power Del.*, vol.31, no.1, pp. 294-302, Feb. 2016.

[23] Y. M. Yeap, A. Ukil, "Fault detection in HVDC system using short time fourier transform," *IEEE Power and Energy Society General Meeting*, Boston, USA, 2016, pp. 1-5.

[24] M. Kong, X. Pei, H. Pang, J. Yang, et al, "A lifting wavelet-based protection strategy against DC line faults for Zhangbei HVDC Grid in China," presented in 19th *European Conf. on Power Electron. and Applica. (EPE'17 ECCE Europe)*, Warsaw, Poland, Sep. 2017, pp. 1-11.

[25] P. Zhao, Q. Chen, K. Sun, "A novel protection method for VSC-MTDC cable based on the transient DC current using the S transform," *International Journal of Electrical Power and Energy Syst.*, vol.97, pp. 299-308, Apr. 2018.

[26] R. Derakhshanfar, T. U. Jonsson, U. Steiger, M. Habert, "Hybrid HVDC breaker–A solution for future HVDC system," *presented in CIGRE Session, Paris*, 2014, pp.1-12.

[27] R. Vidal-Albalate, H. Beltran, A. Rolan, E. Belenguer, R. Pena, and R. Blasco-Gimenez, "Analysis of the performance of MMC under fault conditionsin HVDC-based off-shore wind farms," *IEEE Trans. Power Del.*, vol. 31, no. 2, pp. 839–847, Apr. 2015.

[28] Y. Zhang, N. Tai, B. Xu, "Fault analysis and traveling-wave protection scheme for bipolar HVDC lines," *IEEE Trans. Power Del.*, vol. 27, no. 3, pp. 1583-1591, Jul. 2012.

[29] Y. M. Yeap, N. Geddada, A. Ukil, "Analysis and Validation of Wavelet Transform Based DC Fault Detection in HVDC System," Applied Soft Computing, vol. 61, pp. 127-137, 2017.